ACS APPLIED MATERIALS & INTERFACES

www.acsami.org

Research Article

Correlating Ligand Properties with Photocatalytic Efficiency: A Computational Framework for Interface Engineering

Sohini Khan,[†] Kalyani Patrikar,[†] Ram Sewak, and Anirban Mondal*

Cite This: https://doi.org/10.1021/acsami.5c03069

Read Online

ACCESS | Metrics & More | Article Recommendations | Supporting Information

ABSTRACT: We present the application of the Marcus−Hush formalism as a theoretical framework to investigate charge transfer dynamics in ligand-protected Au systems. By integrating key parameters such as energy level differences and electronic coupling, this approach enables the prediction of photocatalytic efficiency in electron-driven water splitting. Simulations of diverse ligand-functionalized AuNPs establish a clear correlation between charge transfer rates and hydrogen evolution, specifically for functionalized AuNPs bearing aromatic thiols with various para-substituents. Additionally, we extend this framework to selenol-substituted systems, revealing that while selenols perform comparably to thiols in some cases, they do not consistently enhance photocatalytic activity. Beyond electron-driven hydrogen production, we further explore the role of ligand chemistry in modulating hole transfer processes relevant to oxidative half-reactions. In this context, the OH-thiol ligand-functionalized AuNP emerges as the most effective photocatalyst for hole-driven reactions. Overall, this study provides a systematic methodology for screening and designing ligand-functionalized AuNP photocatalysts, offering mechanistic insights into how ligand properties govern photocatalytic performance.

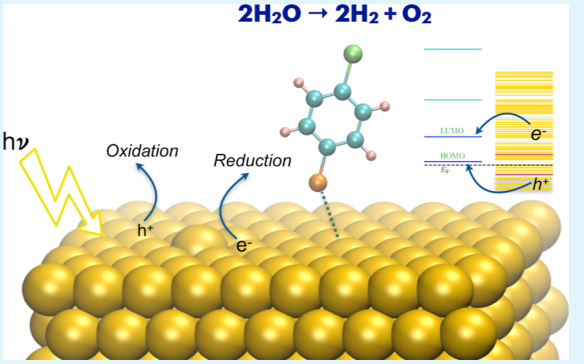

KEYWORDS: *ligand-functionalized gold nanoparticles, photocatalytic water splitting, interface engineering, Marcus−Hush formalism, charge transfer kinetics, electronic coupling, and reorganization energy*

1. INTRODUCTION

Photocatalysts based on gold nanoparticles (AuNPs) have garnered significant attention for enabling efficient redox reactions such as water splitting,[1,2] carbon dioxide reduction,[3] and dye degradation.[4] The interaction of incident light with AuNPs induces surface plasmons, which decay into hot carriers (electrons or holes).[5] These hot carriers can transfer to reaction sites, facilitating the rapid formation of reaction intermediates. Subsequently, the extracted carrier returns to the gold surface during product formation, restoring the catalyst's initial state.[6,7] The efficiency of these photocatalysts hinges on the plasmon decay process and the subsequent transfer of charge carriers from the nanoparticle surface to the reaction site.[8] Surface functionalization through suitable capping layers offers a promising strategy to enhance charge transfer efficiency and plasmon decay into hot carriers.[9−11] Capping layers, such as self-assembled thiol or selenol-based[12,13] ligand monolayers, modulate the chemical interface effect and the energy levels at the nanoparticle surface.[11,14,15] These ligands act as charge transfer mediators, where hot carriers transfer to relevant orbitals on the ligands, resulting in localized charge carriers with extended lifetimes. Such localization enhances photocatalytic efficiency by increasing the likelihood of productive reactions.[16,17]

Despite these advancements, the microscopic mechanisms governing charge transfer from the Au surface to organic molecules remain poorly understood. This knowledge gap hinders the rational design of efficient photocatalysts. Existing studies have observed correlations between physical properties, such as dipole moments and molecular size, and charge transfer efficiency.[18−21] Furthermore, our prior work demonstrated that orbital interactions, quantified through charge transfer integrals, are critical determinants of charge transfer efficiency at organic−inorganic interfaces.[8] Specifically, the energy levels of the ligands' highest occupied molecular orbital (HOMO) or lowest unoccupied molecular orbital (LUMO), along with their coupling to the nanoparticle's states, govern charge transfer dynamics.[22,23] Using first-principles methods such as the projector operator diabatic (POD) method, we have previously shown that the rate of charge transfer, calculated via the Marcus−Hush theory,[24,25] correlates strongly with interface performance in organic photovoltaic devices.

Received: February 13, 2025
Revised: April 25, 2025
Accepted: May 19, 2025

However, these insights have yet to be systematically applied to photocatalysts as a design framework.

In this work, we apply the Marcus−Hush theoretical framework to investigate the mechanism of ligand-functionalized AuNP photocatalysts, focusing on interfacial charge transfer as the rate-determining step. By adapting this classical electron transfer theory to incorporate ligand-induced interfacial effects, we establish a quantitative model that links charge transfer dynamics to photocatalytic performance. We first examine thiol ligands as capping agents for AuNPs in water-splitting photocatalysis, demonstrating a clear correlation between calculated charge transfer rates and experimentally measured hydrogen production rates. Building on these insights, we extend the analysis to selenol-based ligands exhibiting comparable charge transfer kinetics but superior surface adsorption characteristics. Our results suggest that while selenols offer improved stability, specific thiol ligands still enable the highest photocatalytic activity. Overall, this Marcus−Hush-guided approach provides a predictive framework for rational ligand selection in the design of efficient AuNP-based photocatalysts. Although the present study focuses on gold nanoparticles, the methodology is broadly applicable to a wide range of plasmonic and nonplasmonic systems.

2. METHODS

The electronic structure calculations in this study were performed using Density Functional Theory (DFT).[26,27] A single ligand molecule was mounted on a gold slab consisting of 288 atoms arranged in four layers, and the entire system was geometry-optimized. To accurately capture interactions, the top two layers of the gold slab were allowed to move freely, while the bottom two layers were fixed to mimic the bulk structure. The simulation setup and DFT parameters were adopted from ref 28. All calculations were conducted using the Quickstep module of the CP2K program.[29,30] The convergence criteria for nuclear forces were set to 10^{-4} a.u. DFT calculations were performed using a mixed basis set scheme designed to ensure a balance between computational efficiency and accuracy. Gold atoms were described using the TZ-GTH basis set in combination with the Goedecker-Teter-Hutter (GTH) pseudopotentials,[31,32] which are known to accurately account for relativistic effects and electronic delocalization in metallic systems under periodic boundary conditions.[28] For lighter elements (C, H, O, S, Se), the TZVP-MOLOPT-GTH basis set was employed, as it provides reliable accuracy for both molecular and condensed-phase systems.[33,34] To verify the robustness of this mixed basis set approach, we performed convergence tests on representative ligand-AuNP systems (Br−Ph−S−Au and H−Ph−S−Au) using a uniform TZVP-MOLOPT-GTH basis set for all elements. The total energy and force deviations were found to be within 2 meV per atom and 0.01 eV/Å, respectively, confirming the reliability of the mixed basis scheme. This choice is also consistent with our prior studies on similar Au-ligand systems, where the same combination demonstrated stable and accurate performance.[22,23]

Subsequently, the projector operator diabatic method was applied to the optimized stack. The ligand molecule was treated as one block, and the entire Au slab was considered another. Exchange−correlation potentials were described using the generalized gradient approximation (GGA) with the Perdew−Burke−Ernzerhof (PBE) functional.[35] The energy cutoff for the auxiliary plane wave expansion of the charge density was set to 415 Ry. Valence electrons were explicitly modeled, while core electrons were represented using Goedecker−Teter−Hutter (GTH) pseudopotentials.[31,32] A Fermi−Dirac smearing with an electronic temperature of 298.15 K was applied to maintain fractional occupation near the Fermi energy. In the ET_COUPLING module within the PROPERTIES section of CP2K, properties such as energy levels and electronic couplings between the Au slab and the ligand's orbitals were calculated. This choice of PBE functional was guided by prior studies on metal−organic interfaces,[22,23,28] particularly gold−thiol systems, where PBE has demonstrated reliable performance in capturing relative energetic trends and charge transfer characteristics when combined with GTH pseudopotentials and appropriate basis sets. While PBE is known to underestimate electronic band gaps and charge transfer barriers, this work focuses on comparative trends across ligand types rather than on absolute values, making it a suitable choice for extended systems.

Reorganization energies were computed using the four-point method.[36] For each thiol (and selenol), the neutral and charged ground-state geometries were optimized. Single-point energy calculations were then performed for each electronic state at both geometries using Gaussian09,[37] employing the M062X functional with the 6-31+G(d,p) basis set. This level of theory was chosen due to the high sensitivity of reorganization energy to the exchange−correlation functional. M062X is a hybrid *meta*-GGA functional that provides improved accuracy for thermochemical and kinetic properties, particularly in systems involving long-range electron transfer and noncovalent interactions.[38,39] This approach offers a practical compromise between computational cost and reliability, enabling robust estimation of key electron transfer parameters in ligand-functionalized systems.

The overpotential (η) was determined as the difference between the work function of the gold−thiol (or gold−selenol) system and that of pure gold. Work function calculations were performed using DFT implemented in the Vienna Ab initio Simulation Package (VASP).[40] Initial structures were obtained from CP2K optimizations, as discussed above. The GGA-PBE functional was used for exchange−correlation energy modeling.[35] Projector augmented wave (PAW) pseudopotentials were employed to represent all atoms.[41] Plane-wave expansions were truncated at 400 eV, and a gamma-centered Monkhorst−Pack *k*-grid of 5 × 1 × 5 was used for Brillouin zone sampling.[42] van der Waals interactions between adsorbed molecules and the gold surface were included using Grimme's DFT-D3 method with zero-damping.[43] For these calculations, molecules were placed on the gold surface within a vacuum of 20 Å. A single self-consistent field (SCF) cycle was performed with an electronic convergence criterion of 1×10^{-6} eV. The vacuum potential was calculated using the LVHAR tag, which outputs Hartree and ionic potentials. The planar average of these potentials was computed along lattice vectors perpendicular to the surface normal to determine the vacuum potential. The work function was then calculated using the following equation: $\eta = e \times V(\text{vacuum potential}) - E(\text{Fermi level})$.

The rate of charge transfer between the Au slab and the ligand molecule was evaluated using the Marcus−Hush equation[24,25]

$$k_{et} = \frac{2\pi}{\hbar} \int J_E^2(E) \frac{1}{1 + \exp\left(\frac{E - E_F}{kT}\right)} n(E) \frac{1}{\sqrt{4\pi\lambda kT}} \exp\left[-\frac{(\lambda - \Delta E + q\eta)^2}{4\lambda kT}\right] dE \quad (1)$$

Here, J_E represents the coupling between the ligand's orbital (HOMO for hole transfer or LUMO for electron transfer) and the Au states at energy level E, q denotes the elementary charge, with a value of 1.6×10^{-19} coulombs, and $n(E)$ represents the density of states at the energy level E, ΔE is the energy difference between E and the ligand orbital, E_F is the Fermi level, λ is the reorganization energy, η is the overpotential, k is the Boltzmann constant, and T is the temperature (298.15 K).

3. RESULTS AND DISCUSSION

The simulations were conducted for a stack with a single ligand substituent bonded to a gold slab (Figure 1). This approach has been demonstrated in our earlier work[23] to provide an efficient and accurate representation of ligands deposited on gold nanoparticles, owing to the absence of interligand interactions and the periodicity of the Au surface. The study

https://doi.org/10.1021/acsami.5c03069
ACS Appl. Mater. Interfaces XXXX, XXX, XXX−XXX

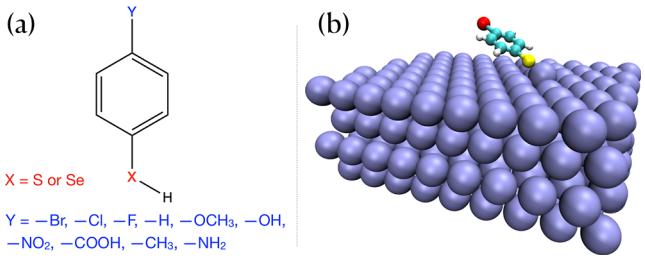

Figure 1. (a) Structures of ligands used as capping agents on the Au surface. Here X = sulfur (−S) for thiol ligands and X = selenium (−Se) for selenol ligands. The substituents considered include bromide (−Br), chloride (−Cl), fluoride (−F), hydrogen (−H), methoxy ($-OCH_3$), hydroxy (−OH), nitro ($-NO_2$), carboxyl (−COOH), methyl ($-CH_3$), and amino ($-NH_2$). (b) Representative AuNP-ligand structure deployed in electronic structure calculations.

focused on aromatic thiol and selenol ligands functionalized with para-position substituents, including methoxy ($-OCH_3$), bromide (−Br), chloride (−Cl), fluoride (−F), hydrogen (−H), hydroxy (−OH), nitro ($-NO_2$), methyl ($-CH_3$), amino ($-NH_2$), and carboxyl (−COOH). The molecular structures of these ligands are illustrated in Figure 1. The sulfur (S) or selenium (Se) atoms in these ligands form weak covalent bonds with the gold surface, effectively capping and stabilizing the nanoparticle system.

Building on the structural overview of the ligands, we now delve into their binding energies on the gold surface, as summarized in Table 1. The calculated binding energies reveal

Table 1. Binding Energies (E_B, in eV) of Thiol and Selenol Ligands with Various Para-Substituents on a Gold Surface[a]

substitution	E_B, thiol	E_B, selenol
$-OCH_3$	−1.55	−1.78
$-NO_2$	−1.77	−1.80
−F	−1.68	−1.81
−Cl	−1.67	−1.79
−Br	−1.66	−1.79
−H	−1.74	−1.84
−OH	−1.61	−1.75
$-NH_2$	−1.55	−1.73
$-CH_3$	−1.70	−1.67
−COOH	−1.75	−1.82

[a]Values indicate stronger adsorption of selenols compared to their thiol counterparts, highlighting the influence of substituents on ligand-surface interactions.

distinct trends for thiols and selenols, with values ranging from −1.55 to −1.77 eV for thiols and −1.67 to −1.84 eV for selenols. This consistent difference highlights the stronger binding affinity of selenols compared to their thiol counterparts across all substituents. The enhanced binding strength of selenols can be attributed to the diffuse nature of selenium's 4p orbitals, which facilitate better overlap with gold's 5d orbitals compared to the more localized 3p orbitals of sulfur. Moreover, according to the HSAB principle,[44] the interaction between gold, a soft acid, and selenium, a softer base due to its larger size and higher polarizability, enhances the binding even further. These findings align with chemical intuition and reinforce the suitability of selenols as robust capping agents.

Analyzing the substituent-specific binding energies, we observe that functional groups such as $-NO_2$, −COOH, and −H exhibit higher binding energies for both thiols and selenols, indicating stronger interactions with the gold surface. In contrast, electron-donating groups like $-NH_2$ and $-OCH_3$ display lower binding energies, suggesting weaker adsorption. The strong binding of $-NO_2$ and −COOH can be attributed to their electron-withdrawing nature, which enhances their interaction with metal. Interestingly, while OCH_3-thiol exhibits the lowest binding energy, likely due to its electron-donating effect repelling the electron-rich Au slab, OCH_3-selenol shows a significantly higher binding energy. This disparity highlights the influence of selenium's softer Lewis base character, which mitigates electrostatic repulsion and allows for stronger interactions despite the +R effect of the methoxy group. As a result, selenols display a narrower range of binding energies compared to thiols. Both $-NH_2$ and $-OCH_3$ introduce excess electron density to the binding atom (S or Se), reducing its affinity for gold and causing unfavorable electrostatic repulsion with the partially negative Au surface. Nevertheless, all ligands exhibit binding energies within a favorable range, reinforcing their potential as effective capping agents for AuNP catalysts.

The density of states (DOS) and the energy level distribution in thiol-based systems provide crucial insights into the charge transfer processes that underpin their catalytic performance. To explore this, we calculated the energy levels of the ligand and gold slab using first-principles methods based on the POD framework. The ligand and gold slab were treated interchangeably as donor and acceptor subsystems to determine their respective energy levels. The results, depicted in Figures 2 and S1, present the molecular orbital energy levels of thiol ligands alongside the electronic states of AuNP. The golden lines denote Au states in these figures, with magenta lines marking the conduction band minimum (CBM) and valence band maximum (VBM). The cyan lines correspond to the ligand's orbitals, where the upper blue line represents the ligand's LUMO, and the lower blue line represents its HOMO. The Fermi level of the combined Au-ligand system is marked by the black dotted line (E_F).

Electron transfer from AuNP to the ligand is initiated by the photoexcitation of an electron from an occupied state of AuNP to one of its unoccupied states, followed by the transfer of this excited electron to the ligand's LUMO. We focused on excitations for an incident 808 nm wavelength, consistent with the experimental conditions for photocatalysis reported in ref 8. Accordingly, unoccupied energy levels up to 1.5 eV above the CBM were considered relevant for charge transfer processes. The maximum energy barrier for electron transfer quantified as the energy difference between the ligand's LUMO and the AuNP's CBM (ΔE_{max}), was calculated for all systems and is summarized in Table 2. This value represents the maximum energy hindrance for electron transfer. Notably, ΔE_{max} varies across ligands, reflecting the influence of substituents. For instance, −OH and $-OCH_3$ thiols exhibit ΔE_{max} values of 0.83 and 0.76 eV, respectively, while electron-withdrawing groups like $-NO_2$ and −COOH yield lower values of 0.51 and 0.61 eV. This trend is attributed to the downward shift of the LUMO energy levels in ligands with electron-withdrawing groups compared to those with electron-donating groups. Halide-substituted thiols (−Br, −Cl, and −F) exhibit similar ΔE_{max} values, approximately 0.7 eV.

While ΔE_{max} provides a measure of the energy barrier, it alone does not fully explain the hydrogen production rates observed experimentally.[8] The charge transfer process at the AuNP-ligand interface is influenced by additional factors,

https://doi.org/10.1021/acsami.5c03069
ACS Appl. Mater. Interfaces XXXX, XXX, XXX−XXX

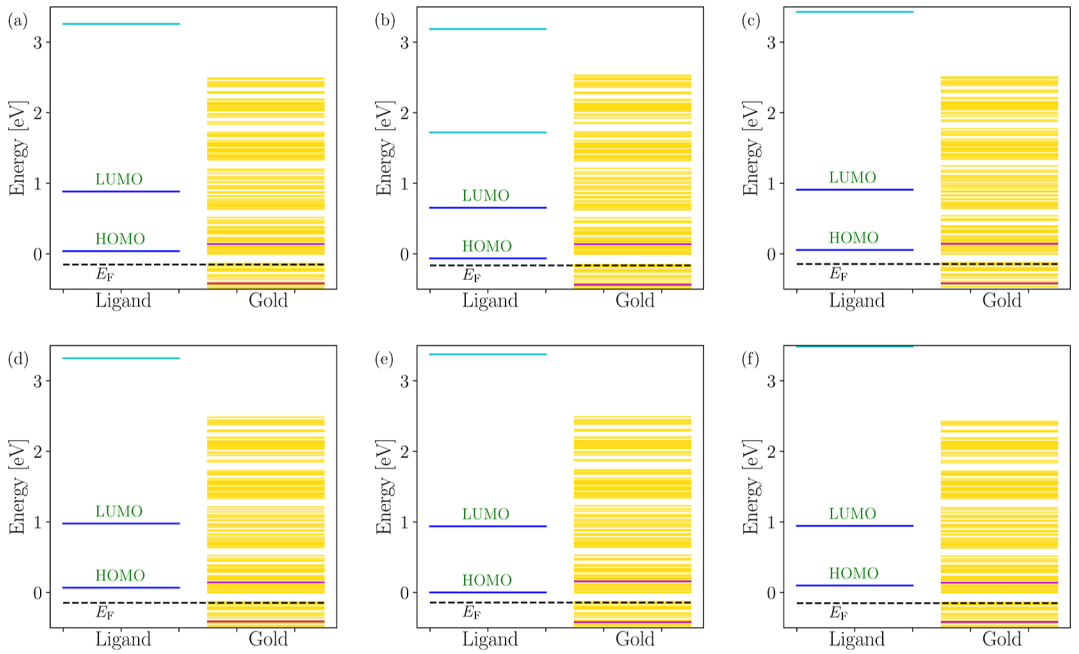

Figure 2. Density of states (DOS) and energy level plots for thiol−Au interfaces with (a) −Br, (b) $-NO_2$, (c) $-OCH_3$, (d) −OH, (e) $-NH_2$, and (f) −H substitutions. Golden lines represent the energy states of Au, with the upper magenta line indicating the conduction band minimum and the lower magenta line marking the valence band maximum. Cyan lines depict the ligand orbitals, where the upper blue line corresponds to the LUMO and the lower blue line to the HOMO of the thiol ligand. The black dotted line denotes the Fermi level of the interface. Similar plots for the remaining thiol−Au interfaces are shown in Figure S1.

Table 2. Energy Difference between LUMO and CBM (ΔE_{max}, eV), J_E at Corresponding E_{max} (J_E^{max}, eV), Work Function (WF, eV), Fermi Energy (E_F, eV), Reorganization Energy (λ_e, eV) for Electron, and Rate of Electron Transfer (k_{et}, s^{-1}) in the Studied Thiol-Based Systems

system	ΔE_{max}	J_E^{max}	WF	E_F	λ_e	k_{et}
$-OCH_3$	0.767	0.074	−0.13	−0.145	0.408	1.40×10^9
$-NO_2$	0.517	0.013	0.07	−0.165	0.888	1.89×10^8
−F	0.748	0.074	−0.07	−0.156	0.396	7.39×10^8
−Cl	0.751	0.083	−0.09	−0.153	0.734	2.81×10^9
−Br	0.746	0.082	−0.11	−0.152	0.540	3.21×10^9
−H	0.805	0.080	−0.13	−0.152	0.925	1.22×10^9
−OH	0.832	0.076	−0.12	−0.146	0.477	1.51×10^9
$-NH_2$	0.781	0.054	−0.15	−0.142	0.555	1.97×10^9
$-CH_3$	0.833	0.076	−0.14	−0.147	0.590	2.61×10^9
−COOH	0.615	0.013	0.03	−0.156	0.842	4.22×10^8

particularly the electronic coupling between the ligand's LUMO and the participating states of AuNP. To quantify this coupling, the charge transfer integral (J_E) was calculated for the relevant states. The results, presented in Figures 3 and S2, depict J_E against the energy difference (ΔE) between the ligand's LUMO and the AuNP unoccupied state. In this way, the points corresponding to minimum ΔE and maximum J_E correspond to the states with the highest feasibility of charge transfer. Hence, a high density of such points tends to make the respective ligands more effective.

The values of J_E span a broad range from 10^{-1} to 10^{-8} eV, reflecting varying degrees of electronic coupling for the AuNP states with the same ligand orbital. While the overall distribution of J_E is similar among ligands, some trends can be observed. For instance, −Br and $-OCH_3$ substitutions tend to have states with the lowest ΔE concentrated at higher J_E values, suggesting relatively stronger coupling. In contrast,

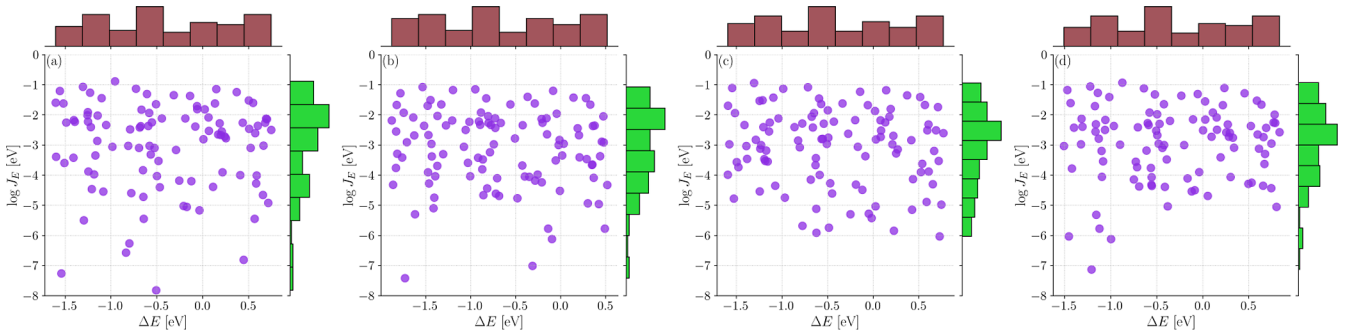

Figure 3. log J_E versus ΔE for electron transfer in (a) −Br, (b) $-NO_2$, (c) $-OCH_3$, and (d) −OH functionalized thiol−Au systems. The *x*-axis represents the energy difference (ΔE) between the ligand's LUMO and the unoccupied states of Au. The *y*-axis shows the logarithm of the charge transfer integral (J_E) between these states. One-dimensional histograms for ΔE and log J_E are displayed along the respective axes. Similar plots for the remaining systems are shown in Figure S2.

https://doi.org/10.1021/acsami.5c03069
ACS Appl. Mater. Interfaces XXXX, XXX, XXX−XXX

ligands such as −COOH show a higher density of states at lower J_E, implying weaker electronic coupling. Among the halogens, −Cl exhibits slightly higher J_E values for states with low ΔE, indicating potentially enhanced charge transfer characteristics.

Building on the analysis of ΔE and J_E distributions, these parameters, along with additional factors, were incorporated into eq 1 to compute the electron transfer rates from AuNP to the ligand. Crucial inputs such as the work function (ϕ) and reorganization energy (λ) were determined from first-principles calculations, with their values provided in Table 2, alongside the Fermi energy for each system. The calculated electron transfer rates were then compared to the experimental hydrogen production rates during water splitting, as reported in ref 8, with the corresponding data summarized in Table S1. A strong correlation between the computed rates and the photocatalyst productivity is evident in Figure 4, demonstrating that higher electron transfer rates correspond to greater hydrogen production. This correlation highlights the combined influence of ΔE, J_E, and other parameters on charge transport efficiency. For instance, while $-NO_2$ exhibits the lowest ΔE_{max}, its broader distribution of states with lower J_E results in a reduced overall rate. Conversely, −Br achieves a high rate despite neither having the lowest ΔE_{max} nor the highest J_E values, owing to the favorable combination of contributing factors. The calculated rate thus provides a holistic measure of the ligand's effectiveness as a capping agent, integrating all key determinants of charge transfer efficiency.

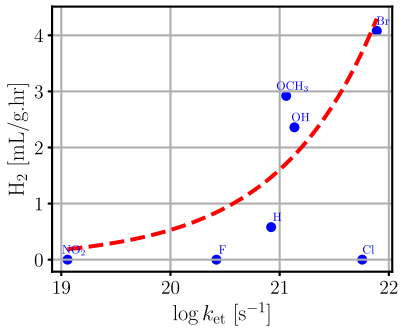

Figure 4. Correlation between experimental hydrogen production and the calculated rate of electron transfer from AuNP to the thiol-based ligands.

The observed strong correlation underscores the pivotal role of charge transport from AuNP to the ligand in dictating the photocatalyst's performance. This finding highlights the rate of charge transport, determined by the physical properties of the interface, as a critical metric for evaluating ligand effectiveness. Consequently, the calculated rate serves as a valuable design guideline for identifying the most suitable substituents to optimize photocatalytic efficiency. An exception to this trend is observed in the case of −Cl, where a high calculated rate does not translate to significant hydrogen production. This discrepancy is attributed to an overestimated reorganization energy (λ), coupled with an unusually high J_E for states with low ΔE_{max}. Notably, the calculated λ for −Cl exceeds those of −Br and −F, deviating from the expected trends among halogens. Such anomalies may arise as artifacts of the computational process. Despite this outlier, the remaining ligands align well with the established correlation between the calculated rate and experimental hydrogen production. Building on this model, we extend our investigation to explore the effect of substituting the thiol group with selenol in these ligands, aiming to assess its impact on photocatalytic performance and further refine our understanding of ligand-substituent interactions. Given selenium's higher polarizability

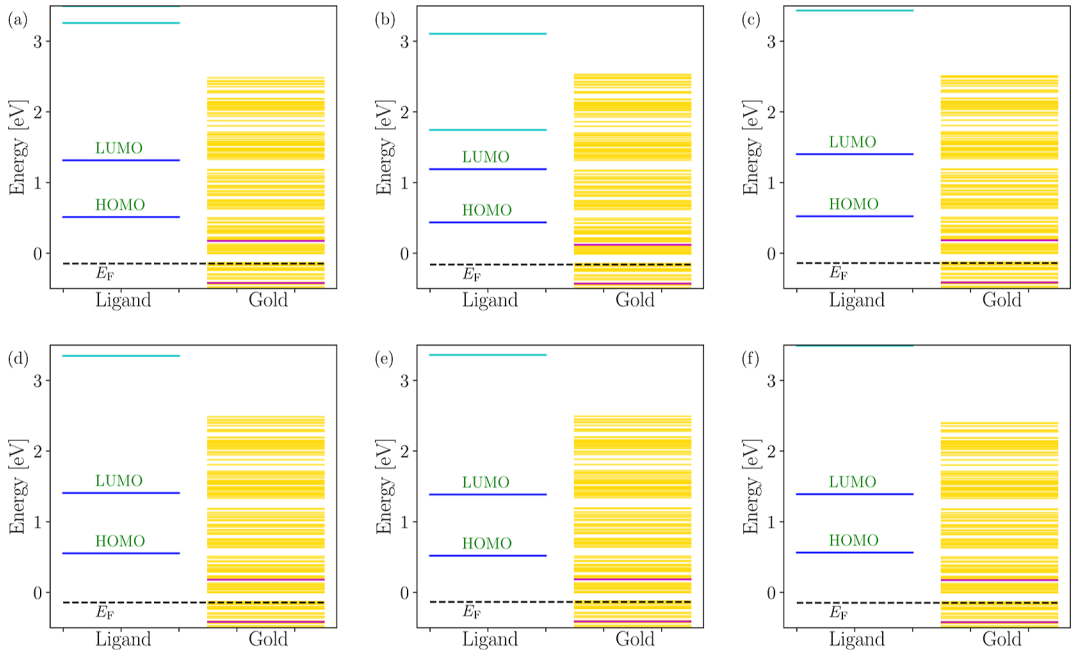

Figure 5. Density of states and energy level plots for selenol-Au interfaces with (a) −Br, (b) $-NO_2$, (c) $-OCH_3$, (d) −OH, (e) $-NH_2$, and (f) −H substitutions. Golden lines represent the energy states of Au, with the upper magenta line indicating the conduction band minimum and the lower magenta line marking the valence band maximum. Cyan lines depict the ligand orbitals, where the upper blue line corresponds to the LUMO and the lower blue line to the HOMO of the thiol ligand. The black dotted line denotes the Fermi level of the interface. Similar plots for the remaining systems are shown in Figure S3.

https://doi.org/10.1021/acsami.5c03069
ACS Appl. Mater. Interfaces XXXX, XXX, XXX−XXX

and more diffuse vacant 4d orbitals compared to sulfur, selenol ligands are also anticipated to exhibit favorable electronic interactions with AuNP that could influence charge transfer dynamics. These characteristics may support enhanced stabilization of charge-transfer states. We compare the electron transfer rates from AuNP to the LUMO of selenol ligands following photoexcitation at a fixed wavelength to examine this.

Energy levels for all selenol systems are presented in Figures 5 and S3, revealing significant shifts compared to their thiol counterparts with the same substituents. For instance, in the case of Br-thiol, ΔE_{max} is 0.7 eV, whereas for Br-selenol, it increases to 1.1 eV (Table 3). Similarly, ΔE_{max} for OCH_3-thiol is 0.7 eV but rises to 1.2 eV for OCH_3-selenol. For NO_2-thiol, ΔE_{max} is 0.5 eV, while the corresponding selenol shows a ΔE_{max} of 1.0 eV. The values of J_E for all selenol systems are illustrated in Figures 6a−d and S4, showing a similar range and distribution of high J_E values as their thiol counterparts. However, a notable difference lies in the density of states near $\Delta E \approx 0.0$ eV, which is higher for thiols than selenols.

Table 3. Energy Difference between LUMO and CBM (ΔE_{max}, eV), J_E at Corresponding E_{max} (J_E^{max}, eV), Work Function (WF, eV), Fermi Energy (E_F, eV), Reorganization Energy (λ_e, eV) for Electron, and Rate of Electron Transfer (k_{et}, s^{-1}) in the Studied Selenol-Based Systems

system	ΔE_{max}	J_E^{max}	WF	E_F	λ_e	k_{et}
$-OCH_3$	1.219	0.012	−0.14	−0.140	0.463	1.51×10^6
$-NO_2$	1.069	0.106	0.01	−0.160	0.884	3.46×10^9
−F	1.167	0.014	−0.12	−0.151	0.685	3.62×10^8
−Cl	1.148	0.026	−0.12	−0.149	0.842	1.32×10^9
−Br	1.140	0.023	−0.12	−0.148	0.782	1.04×10^9
−H	1.216	0.021	−0.14	−0.148	0.909	1.40×10^9
− OH	1.227	0.007	−0.13	−0.143	0.646	1.28×10^8
$-NH_2$	1.200	0.012	−0.15	−0.135	0.770	8.08×10^8
$-CH_3$	1.235	0.007	−0.14	−0.144	0.745	4.78×10^8
−COOH	1.040	0.073	−0.05	−0.150	0.637	3.06×10^8

These differences in energy levels and electronic coupling distributions allow us to classify selenol ligands into two distinct categories based on their ΔE vs log J_E plots. The first category, which includes $-NH_2$ and −H, features states concentrated in the higher log J_E region, spanning from −0.8 to −6 eV. The second category, encompassing all other selenol systems, exhibits a broader distribution, with states extending from −0.8 to −7 eV (Figures 6 and S4). Notably, $-NO_2$ and −COOH selenols stand out within this group, as their states are the most widely spread, extending well into the lower J_E region. This distinction highlights the impact of functional groups on charge transfer characteristics, where variations in electronic structure influence the spread of states and coupling strengths, ultimately shaping the photocatalytic behavior of different selenol ligands.

The key parameters derived from the POD analysis and the final electron transfer rates for all selenol systems are summarized in Table 3. A comparison of the calculated electron transfer rates for thiols and selenols is shown in Figure 6e. Selenol systems generally exhibit charge transfer rates comparable to their thiol analogs with identical substituents, suggesting similar photocatalyst performance. However, thiol systems typically show higher electron transfer rates due to their lower ΔE_{max} values. An exception to this trend is observed for NO_2-selenol, which demonstrates a higher electron transfer rate than NO_2-thiol. Among all systems, Br-thiol exhibits the highest calculated electron transfer rate, making it the most promising candidate for achieving optimal photocatalyst performance in electron-driven reactions.

Although selenol-functionalized ligands exhibit stronger binding to Au nanoparticles, their charge transfer rates remain comparable to or lower than those of thiol systems. This highlights that binding energy, while indicative of thermodynamic stability and effective surface anchoring, does not directly govern charge transfer kinetics. The latter depends primarily on the electronic coupling between ligand orbitals and Au states, the alignment of energy levels, and the reorganization energy associated with electron transfer. Stronger binding does not necessarily optimize these factors simultaneously. In the case of selenol systems, despite their robust surface attachment, the electronic coupling and reorganization energies do not jointly favor accelerated charge transfer, underscoring the need to treat structural stability and kinetic efficiency as distinct descriptors when designing photocatalytic interfaces.

The discussion now shifts to the hole transfer rates from AuNP to the ligands in thiol and selenol systems, providing a comparative analysis to complement the earlier insights into electron transfer. The rates of hole transfer were calculated using eq 1, with J_E determined between the participating states of AuNP and the HOMO of the ligand, and λ calculated specifically for hole transfer. Here, photoexciting an electron from deep-lying states to low-energy unoccupied states of AuNP leaves holes in previously filled states. Hole transfer from AuNP to the ligand corresponds to electron transfer from the HOMO of the ligand to these previously occupied AuNP states, which are up to 1.5 eV below the valence band maximum. Consequently, ΔE is defined as the energy difference between these previously occupied states of AuNP and the ligand's HOMO. Meanwhile, ΔE_{min} represents the energy difference between the VBM and the HOMO, serving as the lowest barrier for hole transfer. The overall charge transfer rate is determined by the interplay between this energy difference and the prefactor involving the reorganization energy (λ) in eq 1.

Figures 7a−d and S5 illustrate the coupling plots for hole transfer in thiols. Figures 7e−h and S6 show the corresponding plots for selenols, where trends are consistent. Examining the ΔE vs log J_E plot for hole transfer in thiols and selenols (Figures 7, S5, and S6), we observe that ΔE values for thiols range from 0 to −2.0 eV, while for selenols, they extend from −0.5 to −2.5 eV. The log J_E values for thiols span from −1.8 to −9 eV, with $-NH_2$, −H, −Cl, $-CH_3$, and −Br predominantly populating the higher log J_E region (within −1.8 to −6 eV). These ligands are expected to exhibit better hole transport than the remaining thiols, where a significant portion of states extends below −6 eV. Notably, NO_2-thiol exhibits the lowest ΔE_{min} (−0.3 eV), with its corresponding Au state displaying a relatively high J_E value (0.044 eV), suggesting that hole transport in NO_2-thiol is significantly more efficient than in other thiol ligands. For selenols, the log J_E range is comparable to that of thiols, but their states are more densely populated in the lower J_E region. In particular, −Br, $-NO_2$, and −H selenols have all their states concentrated within −7 eV, while the remaining selenols have only a few states extending beyond −7 eV.

https://doi.org/10.1021/acsami.5c03069
ACS Appl. Mater. Interfaces XXXX, XXX, XXX−XXX

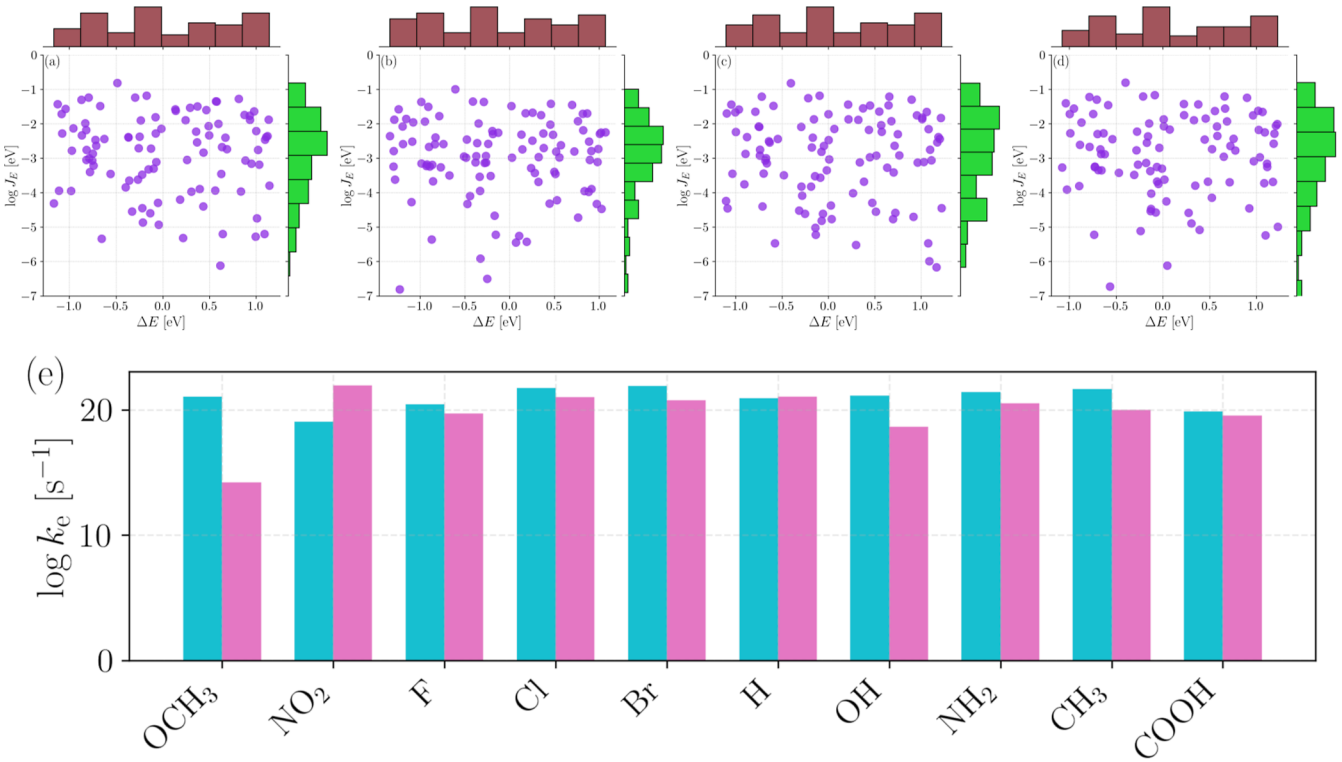

Figure 6. Top panel: log J_E versus ΔE for electron transfer in (a) −Br, (b) $-NO_2$, (c) $-OCH_3$, and (d) −OH functionalized selenol-Au systems. The *x*-axis represents the energy difference (ΔE) between the ligand's LUMO and the unoccupied states of Au. The *y*-axis shows the logarithm of the charge transfer integral (J_E) between these states. One-dimensional histograms for ΔE and log J_E are displayed along the respective axes. Similar plots for the remaining systems are shown in Figure S4. Bottom panel: (e) Comparison of electron transfer rates between Au and ligands for thiol and selenol systems. Bars in magenta represent the rates for selenol-Au interfaces, while bars in cyan represent the rates for thiol−Au interfaces.

The parameter values and rates for both thiols and selenols are provided in Tables S2 and S3, with Figure 7i summarizing the hole transfer rates. In general, hole transfer rates for thiols and selenols with the same substituent are comparable, though notable differences arise in certain cases. For instance, selenols often exhibit lower rates, which can be attributed to variations in electronic coupling and density of states. An exception is the −COOH ligand, where the selenol achieves a slightly higher rate than the thiol, likely due to a higher density of states with large J_E values and fewer states with low J_E. Conversely, NO_2-selenol exhibits a significantly lower rate, which may be linked to a reduced number of strongly coupled states. Among all systems, the photocatalyst with the OH-thiol ligand achieves the highest rate of hole transfer, demonstrating its potential for enhanced productivity in hole-driven reactions.

The reduced number of states near $\Delta E \approx 0$ observed for selenol-functionalized systems arises from a more pronounced ligand-induced shift in the AuNP electronic states, which positions the frontier orbitals of the selenol-ligand assemblies higher relative to the Fermi level compared to thiol systems. This shift limits the density of resonant Au states available for charge transfer. Although selenium's diffuse orbitals could influence electronic coupling, our calculated charge transfer integrals (J_E) show no significant deviation from thiol systems, suggesting that the primary factor behind the slower transfer rates is the reduced density of resonant states rather than diminished orbital overlap. Additionally, while binding energies provide insights into thermodynamic stability, a more comprehensive assessment—such as desorption energies under irradiation—would offer a clearer picture of photocatalyst durability, which we identify as an important direction for future work.

This study underscores the utility of a unified approach to encapsulate all parameters influencing electron and hole transfer into a single equation, offering a comprehensive metric for assessing the photocatalytic efficiency of a surface. While previous studies have examined these parameters individually, this work represents a significant advancement by integrating them into a cohesive framework that directly correlates with the rate of hole or electron transfer and, consequently, the overall photocatalytic rate. This holistic perspective is particularly valuable, as relying on any single parameter can be misleading, as demonstrated in our findings. The application of the Marcus−Hush model not only highlights its robustness but also emphasizes its importance in accurately predicting charge transfer dynamics. This approach paves the way for exploring novel organic molecules designed to enhance the photocatalytic efficiency of noble metal nanoparticles by facilitating charge transfer. By leveraging this unified model, researchers can systematically screen and design materials with optimized charge transfer properties, driving advancements in photocatalysis and related fields.

4. CONCLUSIONS

We have developed a computational framework to evaluate and screen molecules for their photocatalytic efficiency in AuNP-based systems. Within the Marcus−Hush formalism,[24] which integrates key parameters such as energy level differences and electronic coupling between states, we demonstrate a direct correlation between charge transfer

https://doi.org/10.1021/acsami.5c03069
ACS Appl. Mater. Interfaces XXXX, XXX, XXX−XXX

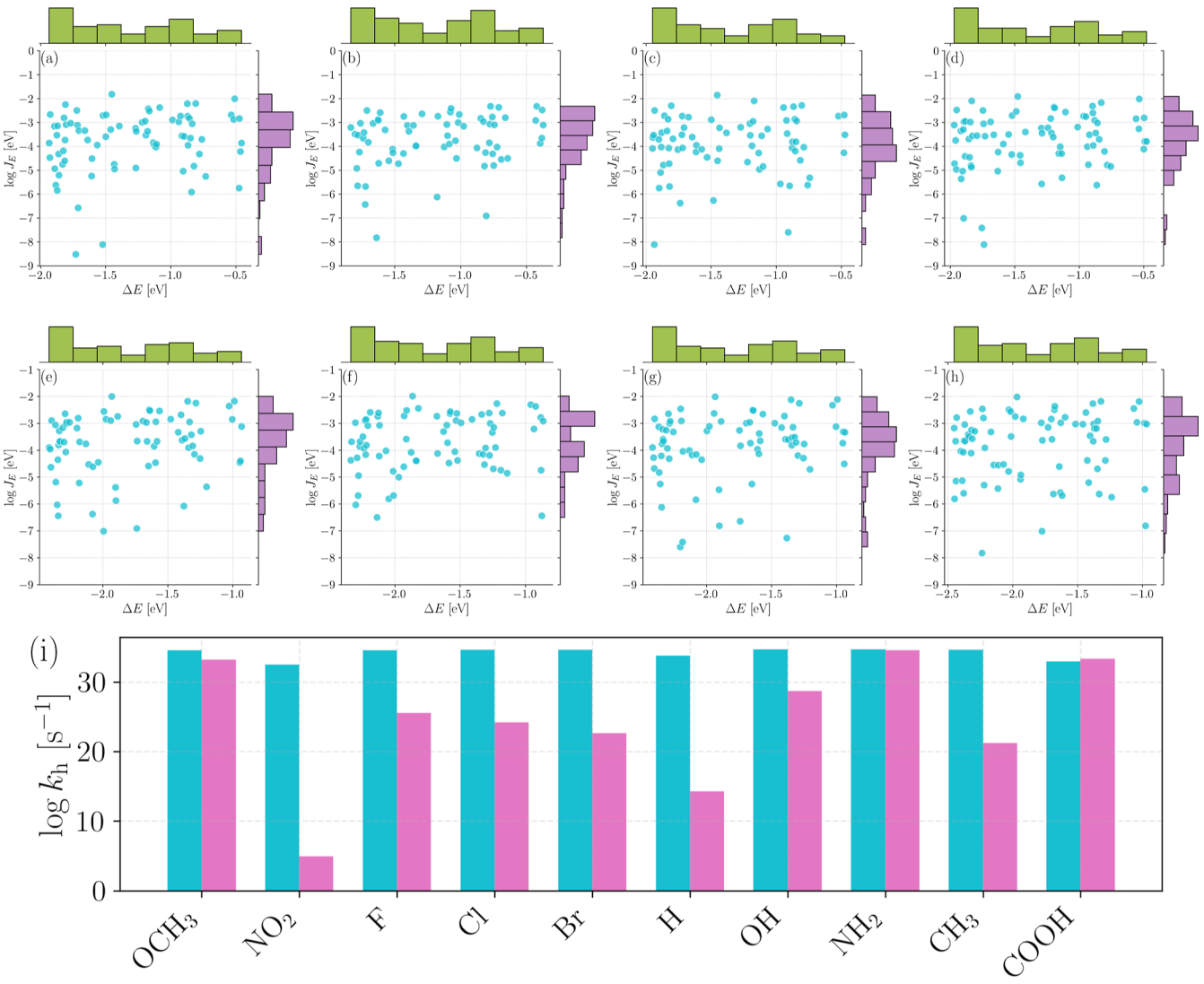

Figure 7. Top row: log J_E vs ΔE for hole transfer in (a) −Br, (b) $-NO_2$, (c) $-OCH_3$, (d) −OH functionalized thiol−Au systems. Middle row: log J_E vs ΔE for hole transfer in (e) −Br, (f) $-NO_2$, (g) $-OCH_3$, (h) −OH functionalized selenol-Au systems. Plotted on the *x*-axis is the difference in energy of previously occupied Au states from VBM and below and HOMO of thiol (or selenol), with the log of charge transfer integral between them on the *y*-axis. The corresponding 1D histogram for each quantity is shown on the axes. Bottom row: (i) comparison of hole transfer rates between Au and ligands for thiol and selenol systems. Bars in magenta represent the rates for selenol-Au interfaces, while bars in cyan represent the rates for thiol−Au interfaces.

rates at the ligand-AuNP interface and the catalytic productivity of AuNP photocatalyst. This model was validated through simulations of diverse para-substituted thiol ligand-functionalized AuNPs, demonstrating its predictive capability. Additionally, the framework was extended to investigate the impact of selenol substitution on photocatalytic performance and to identify efficient ligand capping agents for hole-driven reactions. Our findings reveal that while selenols exhibit comparable performance to thiols in some cases, they do not consistently surpass thiols. Notably, the OH-substituted thiol ligand emerges as the most effective capping agent for AuNP photocatalysts in hole-driven processes.

While the present study focuses on aromatic ligands to enable direct comparison with available experimental data, the proposed framework—based on electronic coupling, energy level alignment, and reorganization energy—is general in nature. As these descriptors are independent of ligand class, the model is expected to apply equally to aliphatic and mixed ligand systems, provided their electronic structure can be reliably determined. Extending this approach to broader ligand families will be the subject of future investigations. Overall, this work highlights the potential of the Marcus−Hush-based model as a powerful tool for rationally designing and optimizing ligand-functionalized photocatalytic systems.

■ ASSOCIATED CONTENT

Data Availability Statement

The data that support the findings of this study are available from the corresponding authors upon reasonable request.

Supporting Information

The Supporting Information is available free of charge at https://pubs.acs.org/doi/10.1021/acsami.5c03069.

contains the density of states, electronic coupling versus energy difference plots, experimental hydrogen production rate, and tables of key interface properties (PDF)

https://doi.org/10.1021/acsami.5c03069
ACS Appl. Mater. Interfaces XXXX, XXX, XXX−XXX

AUTHOR INFORMATION

Corresponding Author

Anirban Mondal − *Department of Chemistry, Indian Institute of Technology Gandhinagar, Palaj, Gujarat 382355, India;* orcid.org/0000-0003-3029-8840; Email: amondal@iitgn.ac.in

Authors

Sohini Khan − *Department of Chemistry, Indian Institute of Technology Gandhinagar, Palaj, Gujarat 382355, India*

Kalyani Patrikar − *Department of Chemistry, Indian Institute of Technology Gandhinagar, Palaj, Gujarat 382355, India*

Ram Sewak − *Department of Chemistry, Indian Institute of Technology Gandhinagar, Palaj, Gujarat 382355, India;* orcid.org/0000-0001-5700-0122

Complete contact information is available at: https://pubs.acs.org/10.1021/acsami.5c03069

Author Contributions

†S.K. and K.P. contributed equally to this work. AM conceived the problem. SK, KP, and RS conducted all the simulations. SK, KP, and AM analyzed the results and prepared the draft.

Notes

The authors declare no competing financial interest.

ACKNOWLEDGMENTS

The authors gratefully acknowledge the Indian Institute of Technology Gandhinagar, India, for providing research facilities and financial support. The authors thank PARAM Ananta for computational resources.

REFERENCES

(1) Tada, H. Overall water splitting and hydrogen peroxide synthesis by gold nanoparticle-based plasmonic photocatalysts. *Nanoscale Adv.* **2019**, *1*, 4238−4245.

(2) Moon, C. W.; Choi, M.-J.; Hyun, J. K.; Jang, H. W. Enhancing photoelectrochemical water splitting with plasmonic Au nanoparticles. *Nanoscale Adv.* **2021**, *3*, 5981−6006.

(3) Chen, L.; Wang, Y.; Yu, F.; Shen, X.; Duan, C. A simple strategy for engineering heterostructures of Au nanoparticle-loaded metal−organic framework nanosheets to achieve plasmon-enhanced photocatalytic CO_2 conversion under visible light. *J. Mater. Chem. A* **2019**, *7*, 11355−11361.

(4) Mondal, S.; Reyes, M. E. D. A.; Pal, U. Plasmon induced enhanced photocatalytic activity of gold loaded hydroxyapatite nanoparticles for methylene blue degradation under visible light. *RSC Adv.* **2017**, *7*, 8633−8645.

(5) Ding, D.; Liu, K.; He, S.; Gao, C.; Yin, Y. Ligand-exchange assisted formation of Au/TiO_2 Schottky contact for visible-light photocatalysis. *Nano Lett.* **2014**, *14*, 6731−6736.

(6) Aslam, U.; Chavez, S.; Linic, S. Controlling energy flow in multimetallic nanostructures for plasmonic catalysis. *Nat. Nanotechnol.* **2017**, *12*, 1000−1005.

(7) Cortés, E.; Besteiro, L. V.; Alabastri, A.; Baldi, A.; Tagliabue, G.; Demetriadou, A.; Narang, P. Challenges in plasmonic catalysis. *ACS Nano* **2020**, *14*, 16202−16219.

(8) Joshi, G.; Kashyap, R.; Patrikar, K.; Mondal, A.; Khatua, S. Ligand-mediated electron transport channels enhance photocatalytic activity of plasmonic nanoparticles. *Nanoscale* **2023**, *15*, 16552−16560.

(9) Lee, K. Y.; Lee, Y. W.; Lee, J.-H.; Han, S. W. Effect of ligand structure on the catalytic activity of Au nanocrystals. *Colloids Surf., A* **2010**, *372*, 146−150.

(10) Lu, L.; Zou, S.; Fang, B. The critical impacts of ligands on heterogeneous nanocatalysis: A review. *ACS Catal.* **2021**, *11*, 6020−6058.

(11) Jain, V.; Roy, S.; Roy, P.; Pillai, P. P. When design meets function: the prodigious role of surface ligands in regulating nanoparticle chemistry. *Chem. Mater.* **2022**, *34*, 7579−7597.

(12) Yee, C. K.; Ulman, A.; Ruiz, J. D.; Parikh, A.; White, H.; Rafailovich, M. Alkyl Selenide- and Alkyl Thiolate-Functionalized Gold Nanoparticles: Chain Packing and Bond Nature. *Langmuir* **2003**, *19*, 9450−9458.

(13) Canepa, M.; Maidecchi, G.; Toccafondi, C.; Cavalleri, O.; Prato, M.; Chaudhari, V.; Esaulov, V. A. Spectroscopic ellipsometry of self assembled monolayers: interface effects. The case of phenyl selenide SAMs on gold. *Phys. Chem. Chem. Phys.* **2013**, *15*, 11559−11565.

(14) Savchenko, P.; Zelikovich, D.; Elgavi Sinai, H.; Baer, R.; Mandler, D. The Effect of the Capping Agents of Nanoparticles on Their Redox Potential. *J. Am. Chem. Soc.* **2024**, *146*, 22208−22219.

(15) Sandeep, K.; Manoj, B.; Thomas, K. G. Gold nanoparticle on semiconductor quantum dot: Do surface ligands influence Fermi level equilibration. *J. Chem. Phys.* **2020**, *152*, 044710.

(16) Zhong, J.; Tang, X.; Tang, J.; Su, J.; Pei, Y. Density functional theory studies on structure, ligand exchange, and optical properties of ligand-protected gold nanoclusters: thiolate versus selenolate. *J. Phys. Chem. C* **2015**, *119*, 9205−9214.

(17) Arora, A.; Oswal, P.; Kumar Rao, G.; Kumar, S.; Kumar, A. Organoselenium ligands for heterogeneous and nanocatalytic systems: development and applications. *Dalton Trans.* **2021**, *50*, 8628−8656.

(18) De Boer, B.; Hadipour, A.; Mandoc, M. M.; Van Woudenbergh, T.; Blom, P. W. Tuning of metal work functions with self-assembled monolayers. *Adv. Mater.* **2005**, *17*, 621−625.

(19) Zhang, B.; Chen, J.; Cao, Y.; Chai, O. J. H.; Xie, J. Ligand design in ligand-protected gold nanoclusters. *Small* **2021**, *17*, 2004381.

(20) Fan, F.-R. F.; Yang, J.; Cai, L.; Price Jr, D. W.; Dirk, S. M.; Kosynkin, D. V.; Yao, Y.; Rawlett, A. M.; Tour, J. M.; Bard, A. J. Charge transport through self-assembled monolayers of compounds of interest in molecular electronics. *J. Am. Chem. Soc.* **2002**, *124*, 5550−5560.

(21) Howell, S.; Kuila, D.; Kasibhatla, B.; Kubiak, C.; Janes, D.; Reifenberger, R. Molecular electrostatics of conjugated self-assembled monolayers on Au (111) using electrostatic force microscopy. *Langmuir* **2002**, *18*, 5120−5125.

(22) Patrikar, K.; Rao, V. R.; Kabra, D.; Mondal, A. Understanding the Microscopic Origin of the Contact Resistance at the Polymer−Electrode Interface. *ACS Appl. Mater. Interfaces* **2023**, *15*, 49427−49435.

(23) Patrikar, K.; Mondal, A. Deciphering the microscopic phenomenon behind contact resistances in interlayer functionalized electrodes and organic semiconductors. *Phys. Rev. Mater.* **2024**, *8*, 054606.

(24) Marcus, R. A. On the Theory of Electron-transfer Reactions. VI. Unified Treatment for Homogeneous and Electrode Reactions. *J. Chem. Phys.* **1965**, *43*, 679−701.

(25) Hush, N. S. Adiabatic Rate Processes at Electrodes. I. Energy-charge Relationships. *J. Chem. Phys.* **1958**, *28*, 962−972.

(26) Hohenberg, P.; Kohn, W. Inhomogeneous Electron Gas. *Phys. Rev.* **1964**, *136*, B864−B871.

(27) Kohn, W.; Sham, L. J. Self-Consistent Equations Including Exchange and Correlation Effects. *Phys. Rev.* **1965**, *140*, A1133−A1138.

(28) Futera, Z.; Blumberger, J. Electronic couplings for charge transfer across molecule/metal and molecule/semiconductor interfaces: Performance of the projector operator-based diabatization approach. *J. Phys. Chem. C* **2017**, *121*, 19677−19689.

(29) Hutter, J.; Iannuzzi, M.; Schiffmann, F.; VandeVondele, J. cp2k: atomistic simulations of condensed matter systems. *Wiley Interdiscip. Rev.: Comput. Mol. Sci.* **2014**, *4*, 15−25.

(30) VandeVondele, J.; Krack, M.; Mohamed, F.; Parrinello, M.; Chassaing, T.; Hutter, J. Quickstep: Fast and accurate density functional calculations using a mixed Gaussian and plane waves approach. *Comput. Phys. Commun.* **2005**, *167*, 103−128.
(31) Hartwigsen, C.; Gœdecker, S.; Hutter, J. Relativistic separable dual-space Gaussian pseudopotentials from H to Rn. *Phys. Rev. B* **1998**, *58*, 3641.
(32) Goedecker, S.; Teter, M.; Hutter, J. Separable dual-space Gaussian pseudopotentials. *Phys. Rev. B* **1996**, *54*, 1703−1710.
(33) Schäfer, A.; Huber, C.; Ahlrichs, R. Fully optimized contracted Gaussian basis sets of triple zeta valence quality for atoms Li to Kr. *J. Chem. Phys.* **1994**, *100*, 5829−5835.
(34) Weigend, F.; Ahlrichs, R. Balanced basis sets of split valence, triple zeta valence and quadruple zeta valence quality for H to Rn: Design and assessment of accuracy. *Phys. Chem. Chem. Phys.* **2005**, *7*, 3297−3305.
(35) Perdew, J. P.; Burke, K.; Ernzerhof, M. Generalized gradient approximation made simple. *Phys. Rev. Lett.* **1996**, *77*, 3865.
(36) Berlin, Y. A.; Hutchison, G. R.; Rempala, P.; Ratner, M. A.; Michl, J. Charge hopping in molecular wires as a sequence of electron-transfer reactions. *J. Phys. Chem. A* **2003**, *107*, 3970−3980.
(37) Frisch, M. J.; Trucks, G. W.; Schlegel, H. B.; Scuseria, G. E.; Robb, M. A.; Cheeseman, J. R.; Scalmani, G.; Barone, V.; Mennucci, B.; Petersson, G. A.; Nakatsuji, H.; Caricato, M.; Li, X.; Hratchian, H. P.; Izmaylov, A. F.; Bloino, J.; Zheng, G.; Sonnenberg, J. L.; Hada, M.; Ehara, M.; Toyota, K.; Fukuda, R.; Hasegawa, J.; Ishida, M.; Nakajima, T.; Honda, Y.; Kitao, O.; Nakai, H.; Vreven, T.; Montgomery, J. A., Jr.; Peralta, J. E.; Ogliaro, F.; Bearpark, M.; Heyd, J. J.; Brothers, E.; Kudin, K. N.; Staroverov, V. N.; Kobayashi, R.; Normand, J.; Raghavachari, K.; Rendell, A.; Burant, J. C.; Iyengar, S. S.; Tomasi, J.; Cossi, M.; Rega, N.; Millam, J. M.; Klene, M.; Knox, J. E.; Cross, J. B.; Bakken, V.; Adamo, C.; Jaramillo, J.; Gomperts, R.; Stratmann, R. E.; Yazyev, O.; Austin, A. J.; Cammi, R.; Pomelli, C.; Ochterski, J. W.; Martin, R. L.; Morokuma, K.; Zakrzewski, V. G.; Voth, G. A.; Salvador, P.; Dannenberg, J. J.; Dapprich, S.; Daniels, A. D.; Farkas; Foresman, J. B.; Ortiz, J. V.; Cioslowski, J.; Fox, D. J. *Gaussian 09*. Revision E.01; Gaussian Inc.: Wallingford CT, 2009.
(38) Zhao, Y.; Truhlar, D. G. The M06 suite of density functionals for main group thermochemistry, thermochemical kinetics, noncovalent interactions, excited states, and transition elements: two new functionals and systematic testing of four M06-class functionals and 12 other functionals. *Theor. Chem. Acc.* **2008**, *120*, 215−241.
(39) Chen, Z.; Li, Y.; He, Z.; Xu, Y.; Yu, W. Theoretical investigations on charge transport properties of tetrabenzo [a,d,j,m]-coronene derivatives using different density functional theory functionals (B3LYP, M06−2X, and wB97XD). *J. Chem. Res.* **2019**, *43*, 293−303.
(40) Kresse, G.; Furthmüller, J. Efficient iterative schemes for ab initio total-energy calculations using a plane-wave basis set. *Phys. Rev. B* **1996**, *54*, 11169.
(41) Blöchl, P. E. Projector augmented-wave method. *Phys. Rev. B* **1994**, *50*, 17953.
(42) Pack, J. D.; Monkhorst, H. J. "Special points for Brillouin-zone integrations"—a reply. *Phys. Rev. B* **1977**, *16*, 1748.
(43) Grimme, S.; Antony, J.; Ehrlich, S.; Krieg, H. A consistent and accurate ab initio parametrization of density functional dispersion correction (DFT-D) for the 94 elements H-Pu. *J. Chem. Phys.* **2010**, *132*, 154104.
(44) Garnovskii, A. D.; Osipov, O. A.; Bulgarevich, S. B. The Principle of Hard and Soft Acids and Bases and the Problem of Competitive Coordination in Complex Compounds. *Russ. Chem. Rev.* **1972**, *41*, 341.

https://doi.org/10.1021/acsami.5c03069
ACS Appl. Mater. Interfaces XXXX, XXX, XXX−XXX